ADVANCED OPTICAL MATERIALS
www.advopticalmat.de

High Yield Synthesis of Water-Processable Donor:Acceptor Janus Nanoparticles with Tuned Internal Morphology and Highly Efficient Charge Separation/Transfer

*Yixuan Du, Yue Li, Olha Aftenieva, Takuya Tsuda, Petr Formanek, Tobias A. F. König, and Alla Synytska**

Here, for the first time, the high-yield (87.6%) robust and facile synthesis of water-processable donor–acceptor Janus nanoparticles (JNP) that are of high potential for optoelectronic applications is reported. The water-processable JNPs have easily controlled Janus ratios and are of excellent quality, which is shown by energy-filtered transmission electron microscopy. The JNPs exhibit improved charge separation and transfer properties compared to the conventional donor–acceptor nanoparticles which is characterized via both steady-state and transient photoluminescence spectroscopy. The Janus character of particles allows the combination of two materials into one composite and programs morphology of structures, which can be formed on the basis of the particles. Finally, outstanding performance of JNP-based photovoltaic cells with 53% improvement of efficiency is shown.

1. Introduction

In recent years, organic semiconductor nanoparticles dispersed in aqueous solvents, have attracted significant interest given that they are environmentally friendly and amenable for large-scale manufacturing.[1] The organic donor:acceptor nanoparticles (D:A NPs) prepared recently by Kosco et al. show significantly enhanced photocatalytic activity in the hydrogen evolution reaction, which indicates those particles exhibit great potential as photocatalysts.[2] In particular, the D:A NPs dispersed in water have been successfully applied in organic photovoltaics (OPVs) in the past decade.[3] Most importantly, the D:A NPs based OPVs have recorded the highest power conversion efficiency (PCE) 7.5% among all of the water-processed OPVs devices, that shows great potential for environmentally friendly applications.[4]

Many factors such as ambient environment, solvent evaporation rates, and solution concentration during the fabrication process affect the active layer morphology of bulk heterojunction (BHJ) OPVs, which makes their fabrication complicated and less reliable. In contrast, structured D:A nanoparticles used as building blocks of BHJs provide an excellent alternative opportunity for tailoring D:A domain size at the nanoscale. In the OPVs system, the domain size of D/A parts should be confined into 5–30 nm range due to the limited exciton lifetime and its short diffusion length.[5] The small domain size ensures excitons reach the D–A interface and dissociate efficiently.[6] Therefore, the D:A nanoparticles should be prepared within nanoscale. At the same time, this requirement causes difficulty to control their internal morphology and design them with a high yield.

To prepare D:A NPs at nanoscale, the mini-emulsion method is considered as the most promising approach. Generally, the NPs are fabricated by evaporating the organic solvent from the emulsion and stabilized by surfactants. Usually, an acceptor-rich core and donor-rich shell would be the typical structure through this methodology.[7] The belief was that the core–shell structure would impede the exciton dissociation and charge separation resulting in a lower efficiency compared to a typical BHJ structure.[8] However, more recent publications presented fabrication of other D:A NP structures to improve the device efficiency.[3c,9] For instance, it was shown that D:A NPs in homogenous and inverted core–shell[10] structures (donor-rich core and acceptor-rich shell) exhibit better performance than conventional core–shell structures. These studies demonstrated that the internal structure of D:A NPs plays a crucial role in their final performance in applications.

Another challenge is the characterization of the donor and acceptor distribution inside of a D:A nanoparticle. Generally, transmission electron microscopy (TEM) is the common technique for the characterization of morphology at a nanometer

Y. Du, Y. Li, O. Aftenieva, T. Tsuda, P. Formanek, T. A. F. König, A. Synytska
Leibniz-Institut für Polymerforschung Dresden e.V.
Hohe Str. 6, 01069 Dresden, Germany
E-mail: alla.synytska@uni-bayreuth.de
Y. Du, A. Synytska
Fakultät Mathematik und Naturwissenschaften
Technische Universität Dresden
Mommsenstrasse 4, 01064 Dresden, Germany
T. A. F. König
Center for Advancing Electronics Dresden (cfaed)
Technische Universität Dresden
01062 Dresden, Germany
A. Synytska
Bayerisches Polymerinstitut – BPI
Universität Bayreuth
Universitätsstraße 30, 95440 Bayreuth, Germany

DOI: 10.1002/adom.202101922

scale. However, there is little contrast for typical materials of photoactive layers through normal bright-field mode.[11] The energy-filtered TEM (EFTEM) technique, utilizing the elemental difference in a multi-component system, seems to be a good choice to provide material contrast in many situations. It has been successfully applied to create spectroscopic contrast between D:A in BHJ structure as well as D:A NPs.[11,12]

This is the first study on the rational design of high-quality D:A Janus NPs (JNPs) with controlled Janus ratios. In this work, we address the challenges in the controlled design of D:A NPs with tunable internal structures and distribution between donor and acceptor parts. It ensures excitons reach the D:A interface and achieve efficient dissociation. Furthermore, EFTEM and photoluminescence spectroscopy are carried out to verify the internal morphology and excellent charge separation properties of D:A NPs. Finally, we correlate the internal morphological studies with the corresponding NP-based polymer solar cells (PSCs) performance and compare their properties to reference devices processed from halogenated solvents.

2. Results and Discussion

The low bandgap conjugated polymer poly({4,8-bis[(2-ethylhexyl)oxy]benzo[1,2-b:4,5-b′]dithiophene-2,6-diyl}{3-fluoro-2[(2ethylhexyl)carbonyl]thieno[3,4 b]thiophenediyl}) (PTB7) was selected as the polymer donor and was matched with a fullerene acceptor [6,6]-phenyl-C_{71}-butyric acid methyl ester ($PC_{71}BM$) were chosen in this work. Their chemical structures are shown in **Figure 1**a. The pure PTB7 and $PC_{71}BM$ nanoparticles are

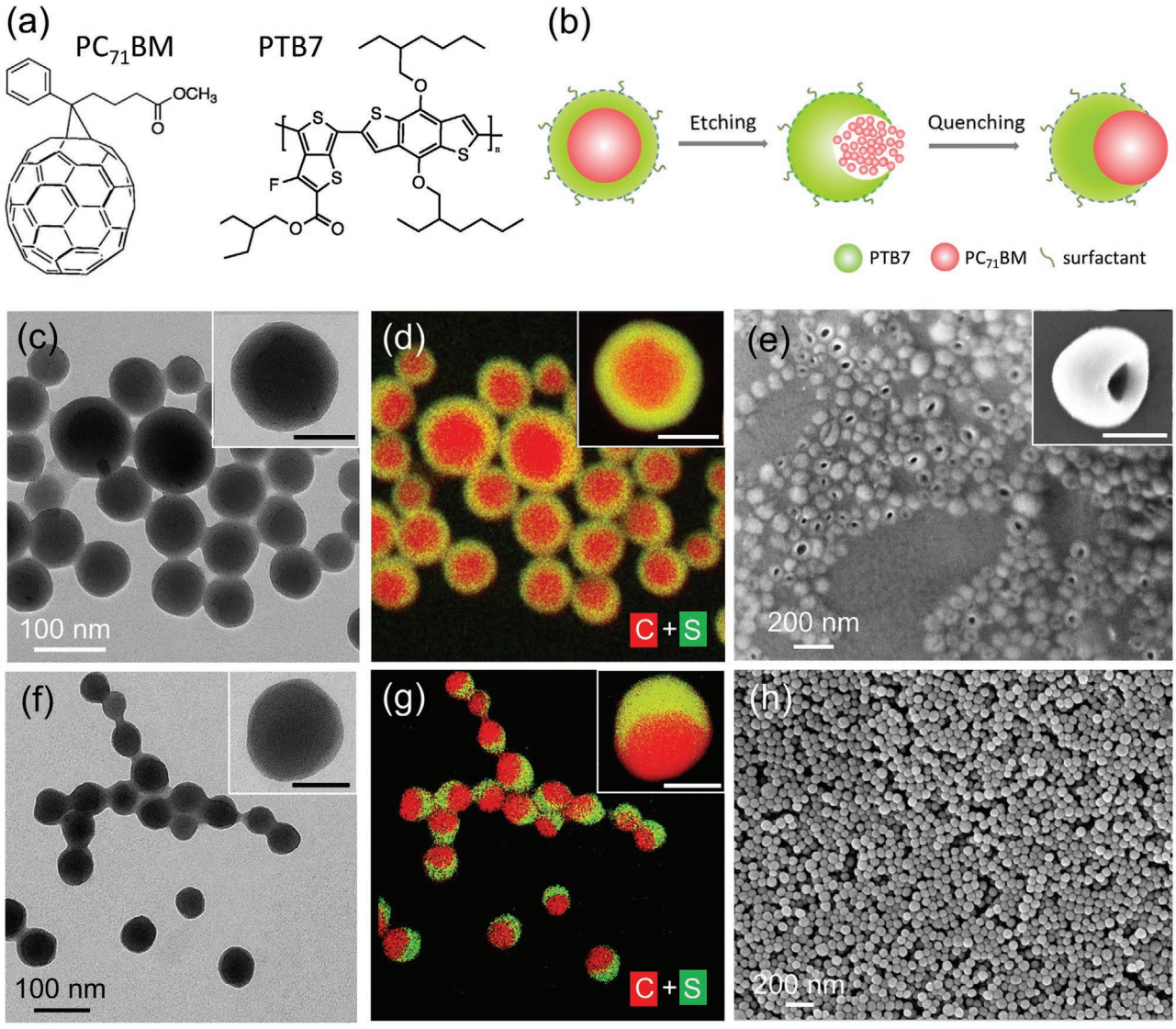

Figure 1. a) Chemical structures of $PC_{71}BM$ (A – acceptor) and PTB7 (D – donor); b) schematic representation of the synthesis route of PTB7:$PC_{71}BM$ Janus nanoparticle in the dispersions; c) bright-field TEM images and d) color-coded elemental EFTEM maps of $PC_{71}BM$-c:PTB7-s NPs of a representative area (inset: single particle; the PTB7 part is in yellow because it contains both of carbon (red) and sulfur (green) elements). e) SEM images of hollow (half-moon) NPs; f) bright-field TEM images; and g) corresponding EFTEM maps of PTB7:$PC_{71}BM$ JNPs (inset: single particle); h) SEM image of PTB7:$PC_{71}BM$ JNPs. The scale bar in inset figures: 50 nm.

fabricated via the mini-emulsion process,[13] and characterized by energy-filtered TEM (Figures S1 and S2, Supporting Information, respectively). Samples were prepared by applying 10 µL aqueous dispersion of nanoparticles (1 mg mL^{-1}) on copper grids to measure TEM and EFTEM.

To prepare PTB7:$PC_{71}BM$ NPs, the emulsion of chloroform droplets containing PTB7 and $PC_{71}BM$ were first dispersed in an aqueous solution of sodium dodecyl sulfate (SDS) The fullerene moieties tend to merge in a continuous phase during chloroform evaporation. As a result, the droplets transformed to $PC_{71}BM$-core:PTB7-shell ($PC_{71}BM$-c:PTB7-s) structure when chloroform evaporated completely (Figure S3, Supporting Information). This fullerene–core and polymer–shell structure is common in the mini-emulsion method. Because the polymer phase (PTB7) tends to minimize interfacial tension between the continuous (water) and disperse phases ($PC_{71}BM$) of the emulsion when the organic solvent (chloroform) is evaporated.[2] Therefore, the polymer PTB7 would separate from the surface of the chloroform droplets, eventually forming NPs consisting of a $PC_{71}BM$ core and PTB7 shell.

In fact, it is challenging to determine the structure of PTB7:$PC_{71}BM$ nanoparticles from bright-field TEM images (Figure 1c) due to the lack of contrast in polymeric materials. To explore their internal morphologies, the obtained NPs are investigated by energy-filtered TEM (EFTEM). This technique is based on detecting low atomic number elemental differences in the chemical structures.[14] Sulfur is present in PTB7 while not in $PC_{71}BM$ (Figure 1a and Figures S1 and S2, Supporting Information), thus the contrast in the elemental sulfur map corresponds to donor material. The obvious contrast between donor and acceptor domains is shown through selectively recording energy losses of the desired elements. This powerful EFTEM technique reveals that the $PC_{71}BM$-rich core is surrounded by PTB7 shell in $PC_{71}BM$-c:PTB7-s NP (Figure 1d) The acceptor core and donor shell exhibit obvious phase separation in this core–shell structure.

To the best of our knowledge, there is no other report on the design of high-yield Janus structures of D:A NPs. Most of the previous publications focused on designing D:A core–shell structures. However, the core–shell D:A NPs must undergo the annealing process to break the shell to generate interconnecting pathways.[7b] It is expected that the Janus structures show a certain phase separation of donor and acceptor. This means that donor and acceptor parts can generate a continuous phase to exhibit higher efficiency in organic photovoltaics.

We aim to convert the obtained core–shell structure into Janus structure using the different solubility properties between donor and acceptor materials. $PC_{71}BM$ has a quite high solubility in N-methyl-2-pyrrolidone (NMP) (>21 mg mL^{-1}), while PTB7 can hardly dissolve (<0.1 mg mL^{-1}) (Table S1, Supporting Information).[15] The prepared core–shell structure converts into the hollow structure when a certain amount of NMP (20 vol%) is involved (Figure 1e). In general, a gradually increased pressure will be created inside the shell upon an explosion to the NMP/water mixture. The pressure becomes high enough during a continuous stirring, the spherical symmetry will break while pushing out the $PC_{71}BM$ through the opening hole. It is consistent with the removal of $PC_{71}BM$ core by annealing.[7d]

In detail, the $PC_{71}BM$ core is dissolved and escapes from one side of the nanoparticle, while the PTB7 collapses thus forming the hollow or half-moon structure. A unique large hole with a cavity inside can be clearly observed in the shell of each particle from scanning electron microscope (SEM) images (Figure 1e). For SEM measurement, samples were prepared by applying 10 µL aqueous dispersion of nanoparticles (1 mg mL^{-1}) on silicon wafers. NMP has a quite high boiling point (204.27 °C) and very low vapor pressure (0.29 Torr, 20 °C),[16] that means this solvent is difficult to evaporate (Table S1, Supporting Information). Therefore, a dialysis procedure to remove involved NMP is applied due to its miscibility with water (Figure 1b). Interestingly, the hollow NPs convert back into the spherical morphology after dialysis, to reach the lowest energy configuration (Figure 1f,h).[17] It is concluded that the $PC_{71}BM$ core is not completely dissolved in 20% NMP/water mixture and part of $PC_{71}BM$ is still in the cavity hole.

Eventually, the $PC_{71}BM$ (previously dissolved in NMP) turns into spheres to reduce their surface area.[18] The $PC_{71}BM$ sphere fills into the vacancy part and thus a Janus structure is generated (Figure 1b,g). The domain differences of PTB7 and $PC_{71}BM$ is most pronounced in PTB7:$PC_{71}BM$ JNPs (Figure 1g). Corresponding elemental mapping confirm that the donor and acceptor are well phase-separated in the nanoparticles after NMP removal (Figure 1g and Figure S4, Supporting Information). The EFTEM results show the core–shell and Janus structures of nanoparticles (Figure 1d,g).

Thus, the internal morphology of PTB7:$PC_{71}BM$ nanoparticles can be converted from core–shell to Janus structures by selective dissolution of PCBM by NMP. The obtained core–shell NPs show a high yield (82.8%) resulting from the mini-emulsion process, according to the statistical analysis of EFTEM images (**Figure 2**a). Moreover, these EFTEM images indicate that the PTB7 shell thickness is ≈12.1 ± 3.6 nm, whereas the diameters of individual cores are around 36.2 ± 8.3 nm (Figure 2a).

Remarkably, the JNPs show a significantly high yield (87.6%) (Figure 2b). More EFTEM images (Figure S4, Supporting Information) and large-area SEM images (Figure S5, Supporting Information) give further supports for their high quality and yield. In addition, these JNPs remain highly stable even after four months of storage at 4 °C. The dynamic light scattering (DLS) (Figure S6, Supporting Information) and SEM (Figure S7, Supporting Information) measurements following the extended storage period give a similar size to the original nanoparticles.

Furthermore, the average hydrodynamic size of the pure PTB7, $PC_{71}BM$ NPs is determined by DLS measurements to be 82 and 42 nm, respectively (Figure S8, Supporting Information). The obtained DLS results of $PC_{71}BM$-c:PTB7-s NPs and PTB7:$PC_{71}BM$ JNPs show similar hydrodynamic diameters (≈110 nm).

After synthesis, we investigate the surface properties of the nanoparticles by electro-kinetic measurements (Figure 2c). The $PC_{71}BM$-c:PTB7-s NPs exhibit similar zeta-potential values with that of pure PTB7 NPs. This result indicates that the surfaces of the fullerene core are covered by polymer PTB7. In contrast, PTB7:$PC_{71}BM$ JNPs show the zeta-potential values close to pure $PC_{71}BM$ NPs at the low pH region and close to PTB7 data when pH increases. These results demonstrate that the shell

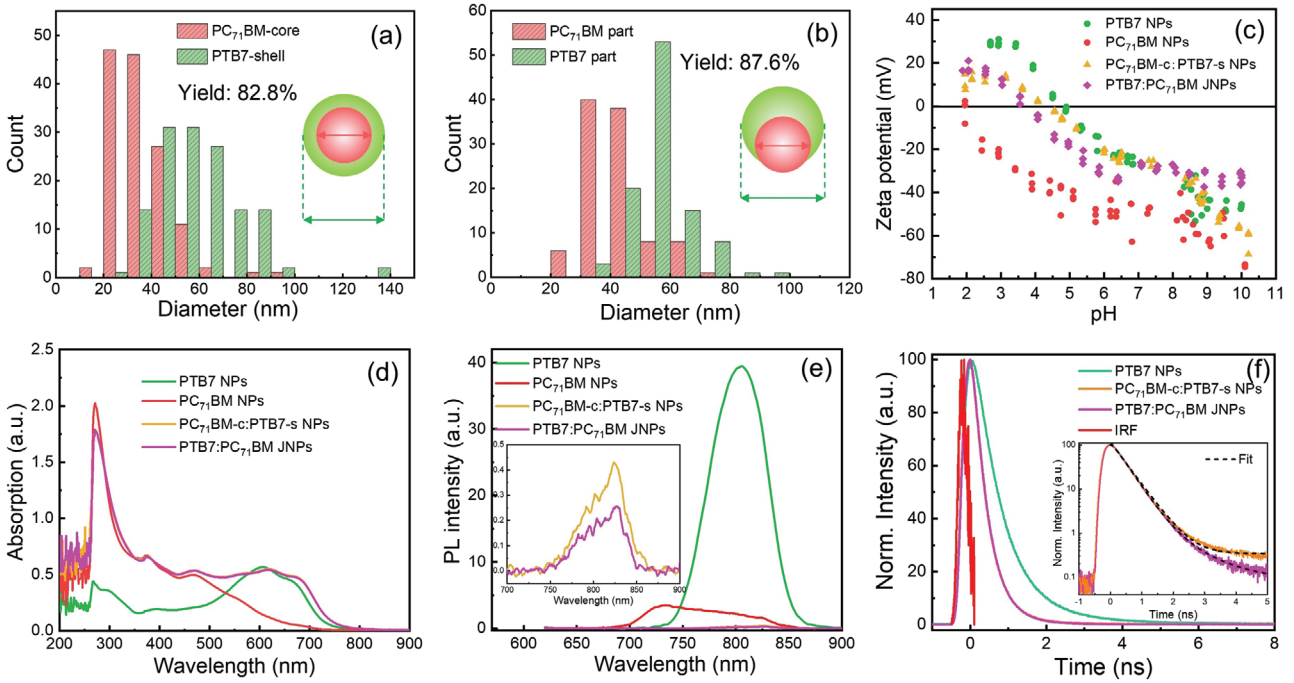

Figure 2. Donor and acceptor size distribution and a corresponding yield of the nanoparticles of a) $PC_{71}BM$-c: PTB7-s NPs and b) PTB7:$PC_{71}BM$ JNPs; c) zeta potential curves versus pH of pristine PTB7, $PC_{71}BM$ NPs, $PC_{71}BM$-c:PTB7-s NPs, and PTB7:$PC_{71}BM$ JNPs (JNPs); d) UV–vis absorption spectra; e) steady-state photoluminescence spectra; and f) time-correlated single-photon counting (TCSPC) emission traces of pure PTB7 NPs, $PC_{71}BM$ NPs, $PC_{71}BM$-c:PTB7-s NPs, and PTB7:$PC_{71}BM$ JNPs dispersed in deionized water (Inset: steady-state magnified PL and data without pristine PTB7 and $PC_{71}BM$ NPs). IRF: instrument response function.

components affect the zeta-potential values. In addition, the corresponding isoelectric point (IEP) values further support this conclusion, summarized in Table S2 (Supporting Information). The pure PTB7 and $PC_{71}BM$ NPs exhibit the highest (4.2) and lowest IEP (2.0), respectively. The values of $PC_{71}BM$-c:PTB7-s NPs, PTB7:$PC_{71}BM$ JNPs are in the middle of pure NPs (Table S2, Supporting Information).

Next, the internal structures of donor and acceptor domains of the NPs were studied by UV–vis spectrophotometry.[8b] For UV–vis absorption, samples were measured in quartz cuvettes, containing 1 mL aqueous dispersion of nanoparticles (0.2 mg mL^{-1}). The single-component NPs show characteristic peaks of $PC_{71}BM$ at the wavelength of 270 nm, whereas a characteristic peak of PTB7 is at 607 nm (Figure 2d). The absorption spectrum of PTB7 is in good agreement with values from the literature.[19] Importantly, the characteristic peaks of PTB7:$PC_{71}BM$ NPs exhibit a redshift from 607 to around 620 nm. This redshift of polymer donor could result from interchain interactions as well as planarization of the polymer chains.[8a] It could be attributed to the formation of aggregates, that is further confirmed by corresponding SEM and bright-field TEM results (Figure S9, Supporting Information). Furthermore, the absorption spectra between $PC_{71}BM$-c:PTB7-s NPs and PTB7:$PC_{71}BM$ JNPs show that there is almost no change in absorption features. The strongest characteristic absorbance peak is observed at 270 nm due to fullerene. In addition, the characteristic peak at 620 nm with a shoulder at 670 nm is ascribed to the semicrystalline PTB7 domains.

Then the photoluminescence (PL) quenching studies are performed on our nanoparticles, which aims to investigate their charge separation behavior (Figure 2e).[7c] The samples (1 mL, 1 mg mL^{-1} of PTB7) were measured in quartz cuvettes in PL characterization. The emission peak of pure PTB7 NPs is at 805 nm. Excellent PL quenching of PTB7 is observed for all structures of D:A NPs. It is ascribed to the formation of an interface between donor and acceptor. Next, the quenching effect between $PC_{71}BM$:PTB7 NPs in different structures is compared to evaluate charge separation properties. The PTB7:$PC_{71}BM$ JNPs show a more obvious PL quenching compared to $PC_{71}BM$-c:PTB7-s NPs, indicating a better charge separation behavior (inset figure in Figure 2e).

To further investigate the charge transfer properties within our D:A NPs, time-correlated single-photon counting (TCSPC) measurements are performed among different NPs (Figure 2f). For TCSPC measurement, the samples (0.2 mL, 1 mg mL^{-1} of PTB7) were characterized in eight-well chambered cover glass. All PL decay curves are well fitted to a mono-exponential decay function (Table S3, Supporting Information). It implies the existence of a simple radiative channel in a two-level system, characterized by a single decay rate.[20] For pure PTB7 NPs, the calculated PL lifetime (τ) is 0.86 ns. As expected, the decay time decreases upon involving $PC_{71}BM$ in NPs (Figure 2f). This indicates the diminishing of the photoluminescent quantum efficiency (PLQE) by 46.5% through an effective and fast charge transfer due to the presence of $PC_{71}BM$ in the NPs.[21] In detail, the PTB7:$PC_{71}BM$ JNPs exhibit the shortest PL lifetime (0.46 ns), compared to $PC_{71}BM$-c:PTB7-s (0.49 ns) (Figure 2f and

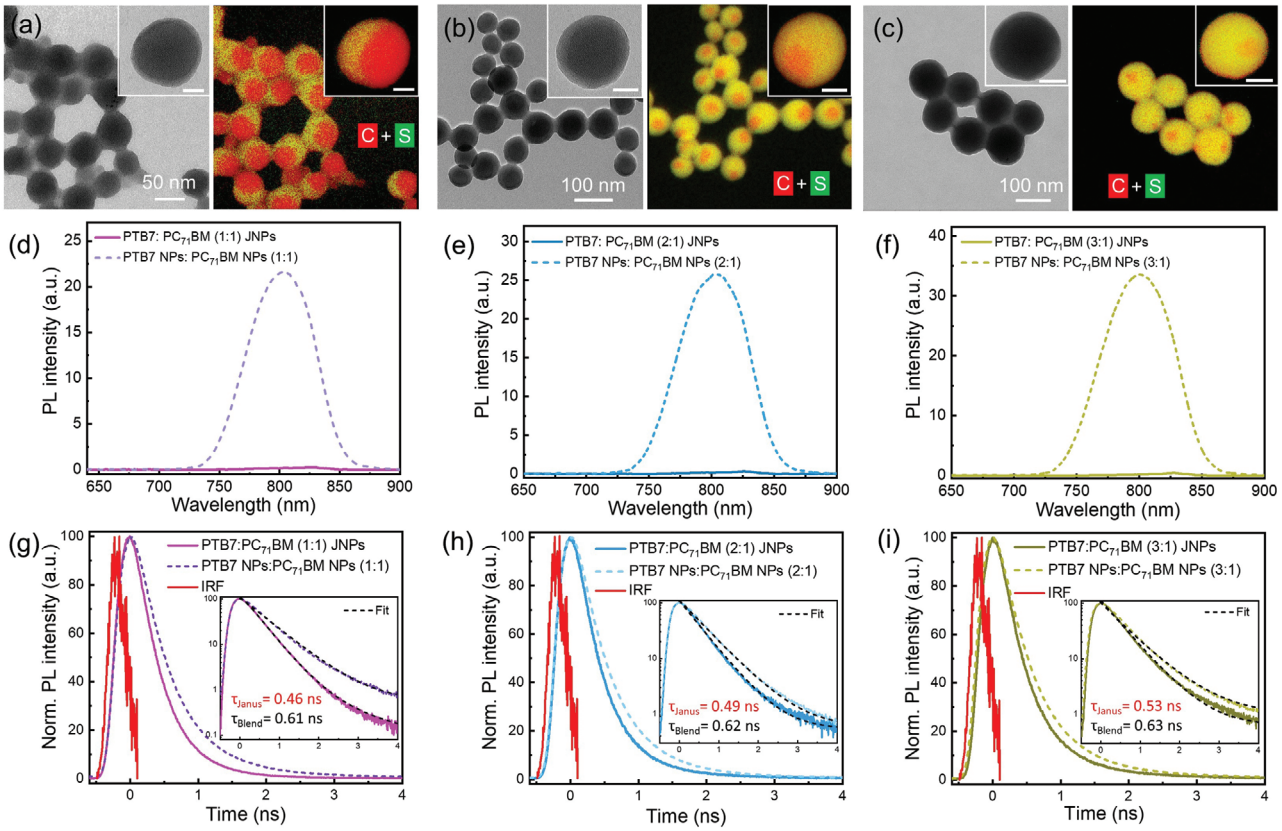

Figure 3. Bright-field TEM images and color-coded elemental (red: carbon; green: sulfur) mappings of PTB7:$PC_{71}BM$ JNPs with different mass ratios: a–c) 1:1, 2:1, and 3:1, respectively (inset image: single Janus nanoparticle; scale bar: 20 nm). Steady-state PL spectra of PTB7:$PC_{71}BM$ JNPs in different Janus ratios: d–f) 1:1, 2:1, and 3:1, respectively, compared with same ratios of mixture of pristine PTB7 NPs and $PC_{71}BM$ NPs. TCSPC decay traces of PTB7:$PC_{71}BM$ JNPs in different Janus ratios: g–i) 1:1, 2:1, and 3:1, respectively, compared with same ratios of mixture of pristine PTB7 NPs and $PC_{71}BM$ NPs (inset: magnified data on log *y*-scale).

Table S3, Supporting Information). This result suggests the efficient charge transfer is related to the internal structure of nanoparticles.[22]

According to previous publications, the electron and hole mobilities strongly depend on the acceptor fraction in D:A blends.[23] Therefore, tuning the D:A ratio is very important to optimize the performance of organic solar cells.[24] In this work, we study various D:A mass ratios (1:1, 2:1, and 3:1) of Janus nanoparticles, in different lobe sizes, and characterize them through EFTEM. (**Figure 3**a–c).

The $PC_{71}BM$ domain is located at the edge of every nanoparticle. In addition, the size of the fullerene part reduces when less amount of fullerene is used (Figure 3a–c). It means that our strategy is demonstrated to fabricate high-yield (87.6%) Janus nanoparticles. As a unique advantage of this procedure, JNPs can be prepared with widely different mass fractions of donor and acceptor and thus control the Janus balance. The PTB7:$PC_{71}BM$ NP morphological differences are attributed to solubility differences as well as to the mass ratios of donor and acceptor. We can control these properties to prepare various internal morphologies on the nanoscale, to exhibit different properties.

Here, we also obtain the zeta-potential curves versus pH of PTB7:$PC_{71}BM$ JNPs among different Janus ratios (Figure S10, Supporting Information). These curves of JNPs trend close to that of PTB7 NPs with an increase of PTB7 ratios. The same tendency is confirmed from obtained IEP results (Table S2, Supporting Information). It indicates that the increase of PTB7 ratios leads to a larger IEP.

To ensure a scientific comparison of PL quenching between PTB7:$PC_{71}BM$ JNPs in different ratios (1:1, 2:1, and 3:1), we control the same concentration of PTB7, which is confirmed by corresponding UV–vis absorption results (Figure S11, Supporting Information). The characteristic peak (at 620 nm) as well as the shoulder (670 nm) of PTB7 exhibit the same intensity among different nanoparticles. On the other hand, the characteristic band of $PC_{71}BM$ shows higher intensity when its mass ratio increases. Afterwards, we investigate the PL behavior between the JNPs and a series of mixtures of pure NPs with various D/A mass ratios (1:1, 2:1, and 3:1) (Figure 3d–f). The emission intensity of the PTB7:$PC_{71}BM$ JNPs is dramatically reduced compared to that of mixed pure donor and acceptor NPs. This result suggests incomplete charge generation and separation in a simple mixed system.

The Janus structure exhibits efficient exciton dissociation, hence quenching the PL emission, even when the PTB7:$PC_{71}BM$ Janus ratio is 3:1 (Figure 3f). The intensity of emission in JNPs decreases slightly as the $PC_{71}BM$ mass ratio increases (Figure S12,

Supporting Information). Moreover, for these two kinds of D:A NPs ($PC_{71}BM$-c:PTB7-s NPs and PTB7:$PC_{71}BM$ JNPs), the emission peak exhibits a redshift compared to pure PTB7 NPs, from 805 to 824 nm, even though they have the similar particle size (Figure S8, Supporting Information). It can be attributed to the radiative recombination of charge transfer states.[25]

The TCSPC delay of JNPs and mixed NPs is exhibited in Figure 3g–i. We notice that JNPs exhibit a much faster decay rate than blended donor NPs and acceptor NPs (Figure 3g–i and Table S3, Supporting Information). This change in PL lifetime is in accordance with the hypothesis of a more efficient charge transfer,[26] signifying a potent electron transfer from the polymer toward the fullerene acceptor in the Janus structure. The latter is due to a higher D/A interface in the Janus structure. Thus, the PTB7:$PC_{71}BM$ JNPs exhibit a superior charge separation behavior, which is beneficial for optoelectronic applications.

Finally, to study the effect of the internal structure of designed NPs in applications, we fabricate polymer solar cells (PSCs) using an inverted device architecture comprising indium tin oxide (ITO)/zinc oxide (ZnO)/ PTB7:$PC_{71}BM$ NPs/ molybdenum trioxide (MoO_3)/silver (Ag) anode (**Figure 4**a). their performances are studied under illumination at AM 1.5G (100 mW cm^{-2}). The Janus ratio 1:1 is applied in this system due to its best photoluminescence properties. The BHJ structured solar cells, formed by spin-coating from either chloroform or chlorobenzene solutions, were prepared as reference. The current density–voltage (J–V) curves of the NPs and BHJ structured PSCs are depicted (Figure 4b) with the key performance parameters (Table S4, Supporting Information). It can be seen that the PTB7:$PC_{71}BM$ NP based devices showed much higher PCE values than BHJ structured PSCs processed from chloroform (0.57%), but still lower than devices processed from more toxic solvent chlorobenzene (Figure 4b and Table S4, Supporting Information). Importantly, PTB7:$PC_{71}BM$ Janus NP devices yield much higher PCE values (2.03%) than the core–shell structured NP cell (1.43%). There is a 53% enhancement, through turning D:A NPs from core–shell into the Janus structures. Among device parameters, J_{SC} of JNPs has been

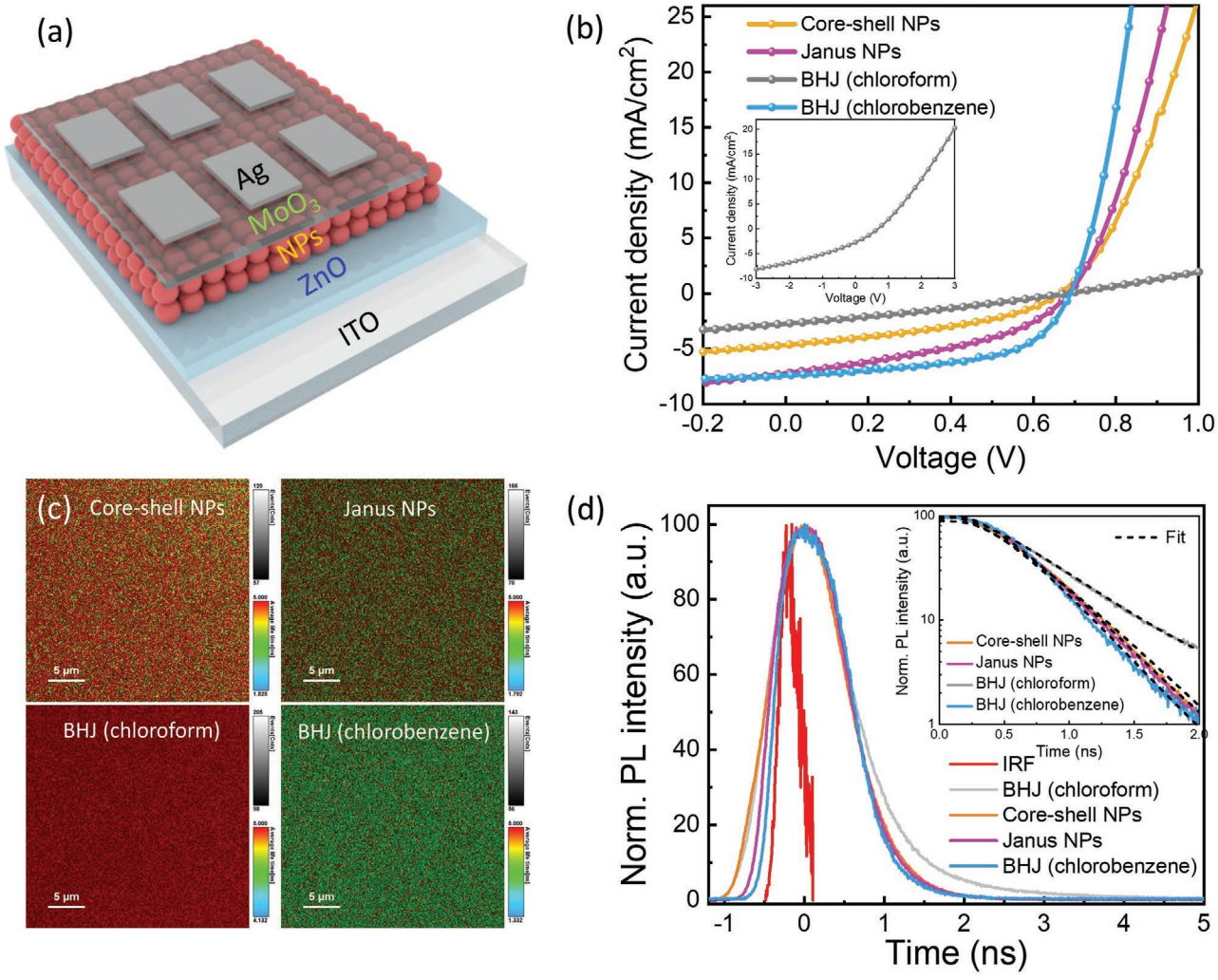

Figure 4. a) Device architecture of NP-based polymer solar cells in this work; b) current density–voltage (J–V) curves of the devices in $PC_{71}BM$-c:PTB7-s NPs, PTB7:$PC_{71}BM$ JNPs in comparison to those of reference devices fabricated from chloroform and chlorobenzene; c) PL lifetime imaging and d) PL lifetime of $PC_{71}BM$-c:PTB7-s NPs, PTB7:$PC_{71}BM$ JNPs and two BHJ structured active layers, respectively.

improved while V_{OC} and FF are constant, indicating the efficient charge transfer of JNPs at D:A interfaces.

PL lifetime imaging was performed to characterize the charge carrier properties of these different structured active layers on a micrometer scale (25 µm × 25 µm) (Figure 4c,d). The chlorobenzene processed film shows the fastest PL decays among these four active layers, followed by the Janus and core–shell NP films. The D:A film processed from chloroform has the longest PL lifetime, resulting from increased exciton recombination.[27] The green region with a short PL lifetime for the chlorobenzene processed BHJ film transits to a red region with a much longer PL lifetime with chloroform. The JNP film shows a larger area in green than that of core–shell NP film, indicating a faster decay rate on average. This indicates more efficient charge transfer in JNP films, leading to a higher current density and thus better device performance. The following TR-PL spectra further support this conclusion (Figure 4d and Table S5, Supporting Information).

3. Conclusions

To summarize this work, we presented a facile and robust route for the synthesis of D:A water-processable nanoparticles with tunable internal morphologies, efficient charge separation, and transfer properties. Internal patchy morphologies could be easily varied between core–shell as well as Janus structures and different Janus ratios. The Janus balance can be easily controlled by synthetically adjusting the D:A mass ratios. To our best knowledge, this is the first report on the fabrication of the D:A JNPs with a remarkably high yield (87.6%) and excellent quality.

The various internal structures of PTB7:PC_{71}BM NPs dramatically improve the charge separation and transfer limitation in D:A dispersions system, verified by PL lifetime and TR-PL decay studies. These PTB7:PC_{71}BM JNPs exhibit the dramatic PL quenching of donors and fast PL decay rates even when the D:A ratio is as high as 3:1. Credited to such excellent charge separation and transfer properties, the JNP-based devices yield PCE 53% that is higher than traditional core–shell NPs. Thus, creating a special patchy morphology with anisotropic Janus topology, that is different from the conventional core–shell design, might allow for a formation of a sharp interface between donor and acceptor domains. In this way, the charge separation and charge transfer properties in single D:A nanoparticles and their assembled structures can be well controlled. Our proposed approach is a promising new strategy to access water-processable JNPs and provides more profound knowledge about the design of high-performance NPs-based PSCs for future optoelectronic applications.

Supporting Information

Supporting Information is available from the Wiley Online Library or from the author.

Acknowledgements

The authors thank Anja Caspari and Martina Priebs for electrokinetic measurements, Fupeng Wu for steady-state photoluminescence measurements. Y.D. acknowledges the financial support from the China Scholarship Council (CSC). The authors thank Benjamin Kohn for proofreading. This project was financially supported by the Volkswagen Foundation through a Freigeist Fellowship to T.A.F.K. The Deutsche Forschungsgemeinschaft (DFG, German Research Foundation) – 404818834 funded the project for O.A. and T.A.F.K.

Open access funding enabled and organized by Projekt DEAL.

Conflict of Interest

The authors declare no conflict of interest.

Data Availability Statement

Research data are not shared.

Keywords

charge separation/transfer properties, donor–acceptor Janus nanoparticles, energy-filtered transmission electron microscopy, optoelectronic applications, steady-state photoluminsecence, transient photoluminescence, water-processable Janus particles

Received: September 23, 2021
Revised: January 17, 2022
Published online: February 27, 2022

[1] a) J. Li, J. Rao, K. Pu, *Biomaterials* **2018**, *155*, 217; b) L. Feng, C. Zhu, H. Yuan, L. Liu, F. Lv, S. Wang, *Chem. Soc. Rev.* **2013**, *42*, 6620; c) D. Tuncel, H. V. Demir, *Nanoscale* **2010**, *2*, 484.

[2] J. Kosco, M. Bidwell, H. Cha, T. Martin, C. T. Howells, M. Sachs, D. H. Anjum, S. G. Lopez, L. Zou, A. Wadsworth, W. Zhang, L. Zhang, J. Tellam, R. Sougrat, F. Laquai, D. M. DeLongchamp, J. R. Durrant, I. McCulloch, *Nat. Mater.* **2020**, *19*, 559.

[3] a) M. J. Griffith, N. P. Holmes, D. C. Elkington, S. Cottam, J. Stamenkovic, A. D. Kilcoyne, T. R. Andersen, *Nanotechnology* **2019**, *31*, 092002; b) Z. Ma, B. Zhao, Y. Gong, J. Deng, Z. a. Tan, *J. Mater. Chem. A* **2019**, *7*, 22826; c) M. Rammal, P. Lévêque, G. Schlatter, N. Leclerc, A. Hébraud, *Mater. Chem. Front.* **2020**, *4*, 2904.

[4] C. Xie, T. Heumuller, W. Gruber, X. Tang, A. Classen, I. Schuldes, M. Bidwell, A. Spath, R. H. Fink, T. Unruh, I. McCulloch, N. Li, C. J. Brabec, *Nat. Commun.* **2018**, *9*, 5335.

[5] a) J. J. Halls, K. Pichler, R. H. Friend, S. Moratti, A. Holmes, *Appl. Phys. Lett.* **1996**, *68*, 3120; b) M. Theander, A. Yartsev, D. Zigmantas, V. Sundström, W. Mammo, M. R. Andersson, O. Inganäs, *Phys. Rev. B* **2000**, *61*, 12957.

[6] F. Zhao, C. Wang, X. Zhan, *Adv. Energy Mater.* **2018**, *8*, 1703147.

[7] a) S. Ulum, N. Holmes, M. Barr, A. L. D. Kilcoyne, B. B. Gong, X. Zhou, W. Belcher, P. Dastoor, *Nano Energy* **2013**, *2*, 897; b) N. P. Holmes, M. Marks, P. Kumar, R. Kroon, M. G. Barr, N. Nicolaidis, K. Feron, A. Pivrikas, A. Fahy, A. D. d. Z. Mendaza, A. L. D. Kilcoyne, C. Müller, X. Zhou, M. R. Andersson, P. C. Dastoor, W. J. Belcher, *Nano Energy* **2016**, *19*, 495; c) H. F. Dam, N. P. Holmes, T. R. Andersen, T. T. Larsen-Olsen, M. Barr, A. L. D. Kilcoyne, X. Zhou, P. C. Dastoor, F. C. Krebs, W. J. Belcher, *Sol. Energy Mater. Sol. Cells* **2015**, *138*, 102. d) N. P. Holmes, K. B. Burke, P. Sista, M. Barr, H. D. Magurudeniya, M. C. Stefan, A. D. Kilcoyne, X. Zhou, P. C. Dastoor, W. J. Belcher, *Sol. Energy Mater. Sol. Cells* **2013**, *117*, 437.

[8] a) F. J. M. Colberts, M. M. Wienk, R. A. J. Janssen, *ACS Appl. Mater. Interfaces* **2017**, *9*, 13380; b) S. Gartner, A. J. Clulow, I. A. Howard, E. P. Gilbert, P. L. Burn, I. R. Gentle, A. Colsmann, *ACS Appl. Mater. Interfaces* **2017**, *9*, 42986; c) S. Subianto, R. Balu, L. de Campo, A. Sokolova, N. K. Dutta, N. R. Choudhury, *ACS Appl. Mater. Interfaces* **2018**, *10*, 44116.
[9] a) S. Lee, D. Jeong, C. Kim, C. Lee, H. Kang, H. Y. Woo, B. J. Kim, *ACS Nano* **2020**; b) J. J. Richards, C. L. Whittle, G. Shao, L. D. Pozzo, *ACS Nano* **2014**, *8*, 4313; c) O. Ghazy, B. Freisinger, I. Lieberwith, K. Landfester, *Nanoscale* **2020**.
[10] a) Y. J. Kim, R. D. Schaller, H. C. Fry, *Small* **2019**, *15*, 1803563; b) M. G. Barr, S. Chambon, A. Fahy, T. W. Jones, M. A. Marcus, A. L. D. Kilcoyne, P. C. Dastoor, M. J. Griffith, N. P. Holmes, *Mater. Chem. Front.* **2021**, *5*, 2218; c) Y. J. Kim, T. D. Loeffler, Z. Chen, S. Sankaranarayanan, *ACS Appl. Mater. Interfaces* **2019**, *11*, 38798; d) S. Chambon, C. Schatz, V. Sébire, B. Pavageau, G. Wantz, L. Hirsch, *Mater. Horiz.* **2014**, *1*, 431.
[11] M. Pfannmöller, H. Flügge, G. Benner, I. Wacker, C. Sommer, M. Hanselmann, S. Schmale, H. Schmidt, F. A. Hamprecht, T. Rabe, *Nano Lett.* **2011**, *11*, 3099.
[12] a) L. D'Olieslaeger, M. Pfannmöller, E. Fron, I. Cardinaletti, M. Van Der Auweraer, G. Van Tendeloo, S. Bals, W. Maes, D. Vanderzande, J. Manca, *Sol. Energy Mater. Sol. Cells* **2017**, *159*, 179; b) S. Zappia, G. Scavia, A. M. Ferretti, U. Giovanella, V. Vohra, S. Destri, *Adv. Sustainable Syst.* **2018**, *2*, 1700155.
[13] V. Percec, *Hierarchical Macromolecular Structures: 60 Years after the Staudinger Nobel Prize II*, Springer, Berlin **2013**.
[14] U. Schlötzer-Schrehardt, K.-H. Körtje, C. Erb, *Curr. Eye Res.* **2001**, *22*, 154.
[15] T. Kumari, S. M. Lee, C. Yang, *Adv. Funct. Mater.* **2018**, *28*, 1707278.
[16] F. Hao, C. C. Stoumpos, P. Guo, N. Zhou, T. J. Marks, R. P. Chang, M. G. Kanatzidis, *J. Am. Chem. Soc.* **2015**, *137*, 11445.
[17] Y. Wang, J. He, C. Liu, W. H. Chong, H. Chen, *Angew. Chem., Int. Ed.* **2015**, *54*, 2022.
[18] Y. Feng, J. He, H. Wang, Y. Y. Tay, H. Sun, L. Zhu, H. Chen, *J. Am. Chem. Soc.* **2012**, *134*, 2004.
[19] C. Stelling, C. R. Singh, M. Karg, T. A. König, M. Thelakkat, M. Retsch, *Sci. Rep.* **2017**, *7*, 42530.
[20] B. Valeur, M. N. Berberan-Santos, *Molecular Fluorescence: Principles and Applications*, Wiley, New York **2012**.
[21] a) F. R. Goßler, A. M. Steiner, O. Stroyuk, A. Raevskaya, T. A. König, *J. Phys. Chem. C* **2019**, *123*, 6745; b) O. Aftenieva, M. Schnepf, B. Mehlhorn, T. A. König, *Adv. Opt. Mater.* **2021**, *9*, 2001280.
[22] Y. J. Kim, P. Guo, R. D. Schaller, *J. Phys. Chem. Lett.* **2019**, *10*, 6525.
[23] R. Pacios, J. Nelson, D. D. Bradley, C. J. Brabec, *Appl. Phys. Lett.* **2003**, *83*, 4764.
[24] C. H. Y. Ho, S. H. Cheung, H. W. Li, K. L. Chiu, Y. Cheng, H. Yin, M. H. Chan, F. So, S. W. Tsang, S. K. So, *Adv. Energy Mater.* **2017**, *7*, 1602360.
[25] a) L. K. Jagadamma, M. T. Sajjad, V. Savikhin, M. F. Toney, I. D. Samuel, *J. Mater. Chem. A* **2017**, *5*, 14646; b) F. Laquai, D. Andrienko, C. Deibel, D. Neher, *Elementary Processes in Organic Photovoltaics*, Springer, Cham **2017**, pp. 267–291.
[26] A. L. Stevens, A. Kaeser, A. P. Schenning, L. M. Herz, *ACS Nano* **2012**, *6*, 4777.
[27] H. H. Fang, L. Protesescu, D. M. Balazs, S. Adjokatse, M. V. Kovalenko, M. A. Loi, *Small* **2017**, *13*, 1700673.